Materials for Renewable and Sustainable Energy (2020) 9:18
https://doi.org/10.1007/s40243-020-00179-1

ORIGINAL PAPER

Nano-sized Pt–NbO_x supported on TiN as cost-effective electrocatalyst for oxygen reduction reaction

N. F. Daudt[1,2] · A. Poozhikunnath[2,3] · H. Yu[2] · L. Bonville[3] · R. Maric[2,3]

Received: 31 March 2020 / Accepted: 1 August 2020 / Published online: 16 August 2020

Abstract

Proton exchange membrane fuel cells (PEMFC) play a key role for sustainable energy; however, catalyst degradation remains one of the main challenges for competing with traditional energy technologies. The Pt/C commercially available electrocatalysts are susceptible to Pt dissolution and carbon support corrosion. In this context, we design a Pt–NbO_x catalyst supported on TiN nanoparticles as an alternative electrocatalyst for the oxygen reduction reaction (ORR). The use of Pt–NbO_x reduces materials' costs by lowering the required platinum loading and improving catalyst performance. The TiN support is selected to improve support stability. The electrocatalyst is successfully synthesized by a one-step flame spray process called reactive spray deposition technology. Electrocatalyst with two different very low Pt loadings (0.032 mg cm^{-2} and 0.077 mg cm^{-2}) are investigated and their performance as cathode is evaluated by the rotating disk electrode method. The new electrocatalyst based on Pt–NbO_x supported on TiN has ORR performance that is comparable to the state-of-the-art Pt/C electrocatalyst. A half-wave potential of 910 mV was observed in the polarization curves, as well as a mass activity of 0.120 A•mg_{Pt}^{-1} and a specific activity of 283 µA•cm_{Pt}^{-2} at 0.9 V. These results demonstrate that Pt–NbO_x on TiN electrocatalyst has the potential for replacing Pt/C cathode in PEMFC.

Keywords PEMFC · Pt–NbO_x electrocatalyst · TiN electrocatalyst supports · Oxygen reduction reaction · Reactive spray deposition technology

Introduction

Proton exchange membrane fuel cell (PEMFC) is known to have outstanding efficiencies, high power density, with the advantage of operating at low temperatures. Therefore, they have attracted huge attention for application in electrical vehicles. However, the major challenges for scaling up this technology and competing with conventional energy conversion technologies remain the high material costs and durability of platinum-based electrocatalysts [1–3]. The poor durability of PEMFC is mainly related to catalyst degradation in the oxygen reduction reaction (ORR) electrode. Until now, commercially available electrocatalysts used in PEMFCs were based on Pt nanoparticles (Pt) and carbon black supports. Catalyst degradation caused by the corrosion of carbon supports and platinum dissolution under fuel cell operation conditions leads to extensive degradation of fuel cell performance [4]. Therefore, highly stable electrocatalysts are required to increase PEMFC long-term performance.

One approach to improve catalyst durability is to replace the carbon support with ceramic-based materials such as titanium oxide [5], niobium-doped titanium oxide [6, 7], niobium oxide [8], titanium nitride [9–11], titanium oxynitride [12] and titanium–niobium nitride [13]. In general, ceramic supports, based on oxide materials, have high corrosion resistance, excellent thermal stability, and low cost. However, their low electrical conductivity is a barrier to their use

Electronic supplementary material The online version of this article (https://doi.org/10.1007/s40243-020-00179-1) contains supplementary material, which is available to authorized users.

✉ N. F. Daudt
natalia.daudt@ufsm.br

[1] Department of Mechanical Engineering, Technology Center, Universidade Federal de Santa Maria, Santa Maria, RS 97105-900, Brazil

[2] Center for Clean Energy Engineering, University of Connecticut, 44 Weaver Road Unit 5233, Storrs, CT 06269-5233, USA

[3] Deparment of Materials Science and Engineering, University of Connecticut, 97 North Eagleville Road, Storrs, CT 06269, USA

in PEMFC [5, 6, 14]. On the other hand, titanium nitride-based materials have much higher conductivity than oxides and are more electrochemically stable and more robust than carbon supports. Therefore, they have been investigated as electrocatalyst supports [10, 11, 15, 16]. Avasarala et al. [4, 15, 16] evaluated the durability and stability of TiN as Pt catalyst support for PEMFC and demonstrated that TiN supports have higher corrosion resistance than carbon supports. However, the overall increase in durability of the electrocatalyst Pt/TiN compared to Pt/C is still inadequate due to Pt agglomeration [15] and, therefore, alternative catalysts are required.

One approach for improving Pt stability is a surface treatment of the TiN nanoparticles to avoid Pt agglomeration. For instance, the preliminary results of Avasarala et al. [15] suggested that a heat treatment in an N_2 atmosphere between 70 and 120 °C increases the oxynitride layer thickness. The oxynitride layer can encapsulate the Pt catalyst reducing Pt particle mobility and agglomeration. This oxynitride layer formed at TiN nanoparticles has conductive nature but it dissolves in acidic electrolytes so that its contribution to decreased electron transport during the initial cycles was minimal. The thermally treated TiN showed an increased stability; however, a relatively lower electrochemical active surface area (ECSA). Shin et al. [17] improved conductivity and durability of TiN supports using a nanotube structure as support for Pt catalysts. The nanotube structure was designed as a grain-boundary free scaffold to reduce ohmic losses. According to Shin et al. [17], the strong metal support interaction (SMSI) positively affected the electrode durability once the electrons moved from the TiN support to Pt 5d band. Furthermore, the TiN surface barely changed after durability tests.

Platinum is the most commonly used electrocatalyst for PEMFC in part due to its excellent catalytic activity. However, the high cost of Pt and its limited availability has restricted the widespread use of PEMFC technology. Alloying Pt with a non-noble metal is an effective strategy for lowering Pt loading, decreasing PEMFC costs, as well as improving ORR activity. Recently, Goshal et al. [18], and Jia et al. [19] demonstrated that platinum and niobium form an alloy with a high potential to enhance ORR activity. Pt interacts with Nb and NbO_x, and Nb contributes to the suppression of Pt dissolution due to strong ligand effects, which enhance catalytic activity toward ORR [19]. Pt–Nb/NbO_x loaded on carbon was tested as an electrocatalyst and demonstrated high activity and durability for both ORR and hydrogen oxidation reaction (HOR) [18]. This new electrocatalyst has significant potential for further improvement but more studies are required to better understand the Pt–Nb and Pt–NbO_x interactions and tailor them to improve the catalyst's performance. A promising approach could be combining the Pt–Nb electrocatalyst with a non-carbon support such as TiN mentioned above.

Methods for the production of Pt-based electrocatalyst including precipitation of Pt [5, 15, 18], microwave-assisted synthesis [20], electrodeposition [21, 22], as well as thin film techniques like magnetron sputtering [8, 23], arc plasma deposition [19], and flame-based processes [24, 25] have been reported. Reactive spray deposition technique (RSDT) has been highlighted as an open-atmosphere, flame-based deposition method because it combines catalyst synthesis and electrode fabrication into a single step. RSDT is a breakthrough process for the deposition of very small catalyst particles (nanoscale) at significantly lower production costs and high efficiency [26, 27]. It also allows the control of the catalyst, support, and ionomer composition; therefore, it is suitable for cost-effective production of low-Pt-loading electrocatalysts [28, 29].

Here, we have investigated Pt–NbO_x supported on TiN as the electrocatalyst for ORR. To the authors' knowledge, this is the first time that such a system is investigated as an electrocatalyst for ORR. The electrocatalyst nanoparticles were synthesized by RSDT. The physical properties were characterized by transmission electron microscopy (TEM), scanning electron microscopy (SEM), inductively coupled plasma optical emission spectroscopy (ICP-OES) and X-ray diffraction (XRD). X-ray photoelectron spectroscopy (XPS) was performed to evaluate the metal–metal and metal–metal oxide interactions on the electrocatalyst surface. The electrochemical performance was evaluated for ORR using rotating disk electrode (RDE).

Experimental

Synthesis of Pt–NbO_x/TiN catalyst

Titanium nitride nanoparticles of an average particle size of 20 nm (97% basis, SkySpring Nanomaterials Inc.), niobium (V) ethoxide (99.95% basis, Sigma-Aldrich), and platinum acetylacetonate (98% basis, Colonial Metals Inc.) were used as precursor materials. The Pt–NbO_x precursor solution was prepared such that the Nb:Pt molar ratio in the final solution is 1:1. The Nb and Pt precursors (0.64 wt% total concentration) were dissolved in a solvent mixture composed of 23.6 wt% methanol (ACS grade, Fisher Scientific) and 59.2 wt% xylene (ACS grade, Fisher Scientific) by sonicating in a bath sonicator for 60 min at room temperature. 16.6 wt% of liquid propane (2.0 grade, Airgas) was then added to the solution. The TiN slurry was prepared by dispersing the TiN nanoparticles along with 0.002 wt% Nafion™ in a solution of isopropanol (ACS, Fisher Scientific) and DI water (1:1 by volume). TiN slurry concentration was 0.5 wt% for 5.5%

Pt–NbO_x/TiN samples and 0.15 wt% for 26.6% Pt–NbO_x/TiN samples.

TiN-supported electrocatalysts were synthesized by RSDT and characterized without any additional processing. A detailed description of the RDST set-up and process can be found elsewhere [27, 30]. Pt–NbO_x loaded on TiN nanoparticles were deposited onto multiple substrates including Nafion™ 211 membranes (Ion Power), polished silicon wafers (Nova Electronic Materials), polypropylene membranes, and 5-mm-diameter hands-free glassy carbon inserts (Pine instruments). The substrates were taped on a 7.5-cm^2 aluminum sample holder as described by Yu et al. [28]. The precursor solution was heated to a set point of 190 °C, and atomized through the primary nozzle of the RSDT at a constant flow rate of 4 mL min^{-1}. The TiN slurry was sprayed through a set of two secondary spray nozzles (Nordson EFD) at constant flow rate of 1.5 mL min^{-1}. A quench ring, flowing air at a flow rate of 100 SLPM was introduced at a distance of 9.7 cm from the primary nozzle to maintain the substrate temperature in the range of 80–100 °C during deposition. Deposition time was 30 min for 5.5% Pt–NbO_x/TiN samples and 120 min for 26.5% Pt–NbO_x/TiN. RSDT parameters are summarized in Table 1. For the deposition of TiN without the catalyst, a precursor solution was prepared using the same solvent composition as the Pt–NbO_x/TiN catalyst, but without the addition of the Pt and Nb precursors to the solvent mix. Unsupported Pt–NbO_x samples (100% Pt–NbO_x in Table 1) were prepared under deposition conditions similar to those of the supported catalysts but without any secondary nozzles spraying TiN. Electrocatalysts deposited on Nafion™ membranes and silicon wafers were used for microstructural characterization, while the material deposited on polypropylene was used for compositional analysis. The film deposited on glassy carbon inserts was used directly for RDE experiments.

Physical characterization

Sample microstructure was characterized by Scanning Electron Microscopy (SEM) using Thermo Fisher Quanta 250 FEG SEM. For the cross section, the analysis on the electrocatalyst layer deposited on Nafion™ membranes was freeze fractured using liquid nitrogen. Sample composition was analyzed by X-ray–energy-dispersive spectroscopy (EDS). Phase composition was investigated by X-ray diffraction (XRD) using Bragg–Brentano geometry (θ–2θ) in a Bruker D8 advance X-ray diffractometer. Lattice constant was calculated using Bragg's law $\left(d_{[111]} = \frac{a_o}{h^2+k^2+l^2}\right)$ for the Bragg's angle of the (1 1 1) diffraction plane of XRD spectra of TiN. The crystallite size was calculated using the following Scherrer equation:

$$B(2\theta) = \frac{K\lambda}{L\cos\theta}, \quad (1)$$

where B is the width of half the diffraction peak, L is the crystallite size, λ is the diffracted wavelength of X-ray (0.154056 nm), K is the Scherrer constant (0.94 for spherical particles), and θ is the diffraction angle.

Particle size and particle size distribution were evaluated by analyzing the transmission electron microscopy (TEM) images with ImageJ software [31]. TEM images were obtained in a Thermo Scientific Talos F200X S/TEM at 200 kV. The distribution of Pt and Nb was analyzed by STEM-EDS mapping using the Super-X EDS system (Bruker). TEM specimen were prepared by dispersing deposited material in spectroscopy grade isopropanol (Sigma-Aldrich) for 30 min using a bath sonicator and putting a 10 µL drop of the dispersed solution on a carbon-coated 3 mm Cu grid (300HD, Pacific Grid Tech). The droplet was covered and allowed to dry overnight under ambient conditions.

The platinum and niobium loadings were determined by ICP-OES using a Perkin Elmer Optima 7300DVICP-OES. The electrocatalyst surface was analyzed by X-ray photoelectron spectroscopy (XPS) using Phi 510 X-ray photoelectron spectrometer (radiation source: Al Kα, $\lambda = 1486.6$ eV). The binding energies reported in this study were charge-corrected using the adventitious carbon 1 s binding energy at 284.8 eV as reference. The XPS data was processed using CasaXPS software (Casa Software Ltd). Micro-Raman spectroscopy was used to examine the TiN support for evidence of partial oxidation. A Renishaw System 2000 with a 785-nm laser source was used for the micro Raman analysis at a spatial resolution of ~ 1 µm.

Table 1 Summary of experimental condition for RSDT

Electrocatalyst	Thickness (µm)	Pt–NbO_x amount (wt%)	PtNb (molar ratio)	Pt loading (mg•cm^{-2})	TiN slurry concentration (wt%)	Deposition time (min)
5.5% Pt–NbO_x/TiN	5	5.5	22.7	0.032	0.5	32
26.6% Pt–NbO_x/TiN	2.5	26.6	6.7	0.077	0.15	60
100% Pt–NbO_x	< 0.5	100		–	0	55
TiN	2.6	0	–	0	0.5	45

Electrochemical characterization

The ORR activity was evaluated using a rotating disk electrode (RDE). The electrochemical measurements were conducted in a custom-designed three-compartment electrochemical cell (Adams & Chittenden Scientific Glass, CA). Nitrogen- or oxygen-purged 0.1 M perchloric acid (double distilled, GFS Chemicals. Inc.) was used as the electrolyte. The potential was determined using the Hg/$HgSO_4$ reference electrode with a potential of 0.72 V vs. RHE. A Pt wire was used as counter electrode. The working electrode was mounted on an MSR rotator (AFM-SRCE, Pine Instruments). A Solartron 1287 potentiostat was used for all measurements. Prior to the measurement, the working electrode was electrochemically cleaned by cycling between 0.0 V and 1.4 V (vs. RHE) at a scan rate of 200 mV s^{-1} for 40 cycles. The polarization curves for ORR were recorded in linear sweep voltammetry scanning from 0.05 to 1.05 V vs. RHE with scan rate of 20 mV s^{-1} [32]. The performance was recorded with rotation speeds of 400, 900, 1600, and 2500 rpm. The background current was measured by running ORR sweep in a nitrogen-purged 0.1 M perchloric acid solution at same protocol applied to collect ORR curves in O_2 statured electrolyte. The background current was subtracted from ORR to eliminate any capacitive current contribution. The high-frequency resistance (HFR) was measured using electrochemical impedance spectroscopy (EIS) recorded at 0.9 V vs RHE with 1600 rpm rotating speed to obtain the iR corrections. Cyclic voltammograms (CVs) were collected in nitrogen-purged cells between 0.05 and 1.2 V (vs. RHE) at a scan rate of 20 mV•s^{-1} for 30 cycles until repeatable (the 5 last cycles overlapped). Only the last cycle is shown. Tafel plots (E versus $\log|J_k|$) were obtained from corrected ORR data collected at 1600 rpm by calculating the kinetic current (I_k) according to the following equation:

$$I_k(\mathrm{A}) = \frac{I_{\lim} XI(\mathrm{A})}{(I_{\lim} - I(\mathrm{A}))}, \tag{2}$$

where $I_{\lim}$ is the measured limiting current (A) and I is the measured current (A).

The electrochemical active surface area (ECSA) was calculated using the CV data collected at a scan rate of 20 mV s^{-1} according to the following equation for hydrogen adsorption:

$$\mathrm{ECSA_{Pt}}\left(\mathrm{m^2 g_{Pt}^{-1}}\right) = \left[\frac{Q_{\text{H-adsorption}}(C)}{210\mu\mathrm{Ccm_{Pt}^{-2}}\left(\mathrm{mg_{Pt}cm^{-2}}\right)A_g\left(\mathrm{cm^2}\right)}\right]10^5. \tag{3}$$

The electron transfer number (n) was calculated by applying the Koutecky–Levich equation as follows:

$$\frac{1}{i} = \frac{1}{i_k} + \left(\frac{1}{0.62nFAD^{2/3}v^{-1/6}w^{1/2}}\right), \tag{4}$$

where A is the geometric area of the disk (cm^2), F is Faraday's constant (C mol^{-1}), D is the diffusion coefficient of O_2 in the electrolyte (cm^2 s^{-1}), v is the kinematic viscosity of the electrolyte (cm^2 s^{-1}), C is the concentration of O_2 in the electrolyte (mol cm^{-3}), ω is the angular frequency of rotation (rad s^{-1}) and the kinetic current (i_k) is the inverse of the intercept of the linear Koutecky–Levich plot with the Y-axis.

The Pt area-specific activity (I_s) was estimated using the kinetic current (I_k) calculated from the linear Koutecky–Levich plots and normalization to the Pt electrochemical surface area using

$$I_s\left(\mu A\ \mathrm{cm_{Pt}^{-2}}\right) = \frac{I_k(\mathrm{A})}{Q_{\mathrm{H=adsorptin}}/210\mu\mathrm{Ccm_{Pt}^{-2}}}. \tag{5}$$

The mass activity was calculating (I_m) according to the following equation:

$$I_s\left(\mathrm{A\ mg_{Pt}^{-1}}\right) = \frac{I_k(\mathrm{A})}{\mathrm{mg_{Pt}}}. \tag{6}$$

More details about the methodology for ECSA analysis and I_s calculation can be found in the literature [32].

Results and discussion

Synthesis and physical characterization of Pt–NbO_x/TiN catalyst

We successfully synthesized Pt–NbO_x/TiN catalyst in a one-step process using RSDT. RSDT was capable of depositing a homogeneous Pt–NbO_x/TiN catalyst layer onto Nafion™ membranes (Fig. 1). A catalyst content of 5.5 wt% with a Pt loading of 0.032 mg cm^{-2} and a thickness of ca. 4.5 µm was obtained using a TiN slurry concentration of 0.5 wt% and a deposition time of 32 min (Fig. 1a, b). By increasing the deposition time to 60 min and decreasing the TiN slurry concentration to 0.15 wt%, an electrocatalyst layer of ca. 3.5 µm thickness, catalyst content of 26.6 wt% with a Pt loading of 0.077 mg cm^{-2} was obtained on Nafion™ membrane (Fig. 1c, d). RSDT deposition of the support TiN nanoparticles (without Pt–NbO_x particles) on Nafion™ resulted in a homogenous layer of ca. 2.6 µm thickness (Fig. 1e, f). In the case of the 100% Pt–NbO_x electrocatalyst deposited on Nafion™ membrane, a rough layer of < 500 nm thickness was obtained (Fig. 1g, h).

Bright-field (BF) TEM images of the Pt–NbO_x (Fig. 2a, b) show a relatively homogeneous dispersion of Pt–NbO_x catalyst particles on TiN support. The average particle diameter was determined to be 1.6 nm with size distribution ranging

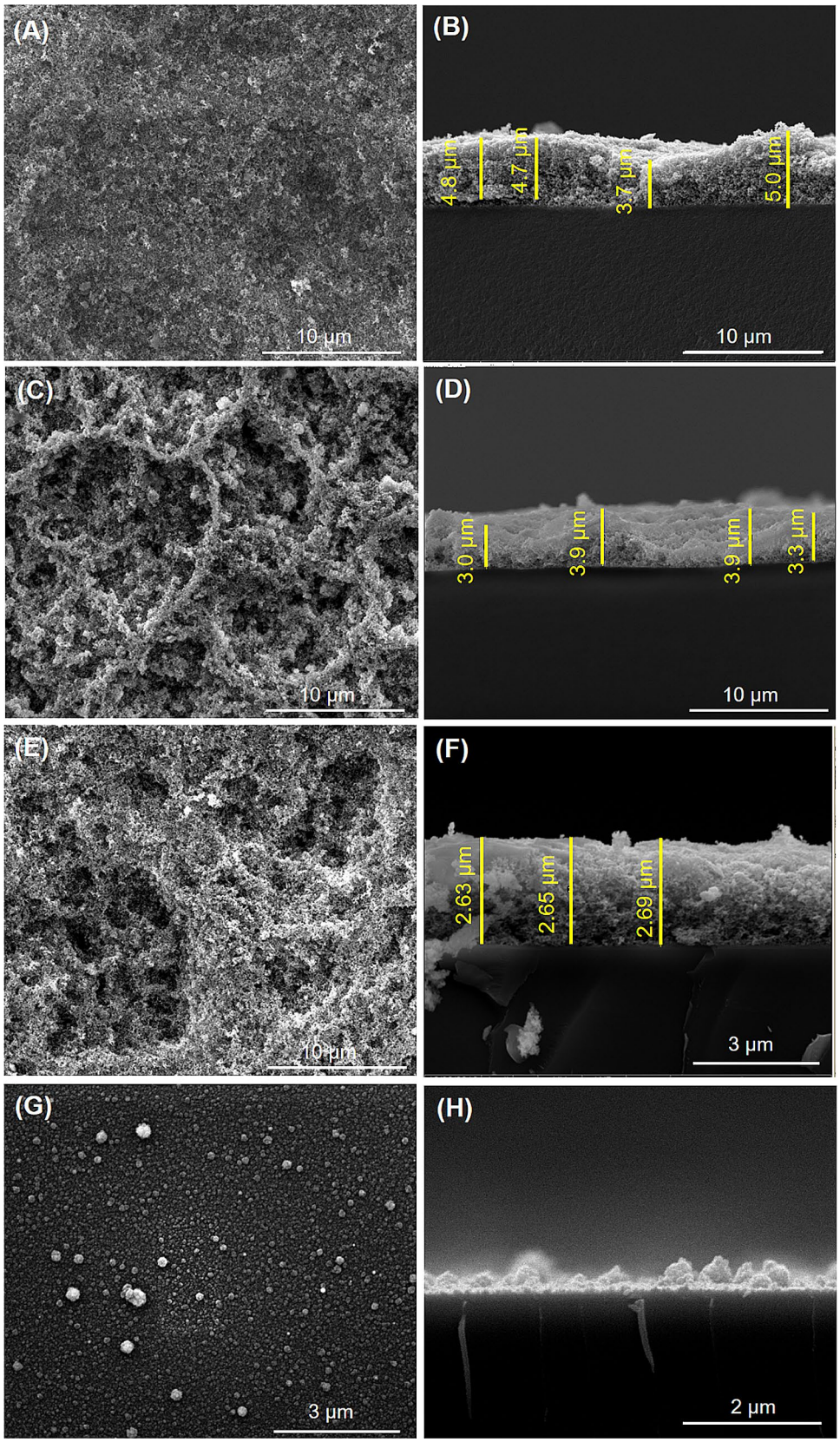

Fig. 1 SEM image of **a** 5.5% Pt–NbO_x/TiN surface and **b** cross section, **c** 26.6% Pt–NbO_x/TiN surface and **d** cross section, **e** TiN surface and **f** cross section and **g** 100% Pt–NbO_x surface and **h** cross section

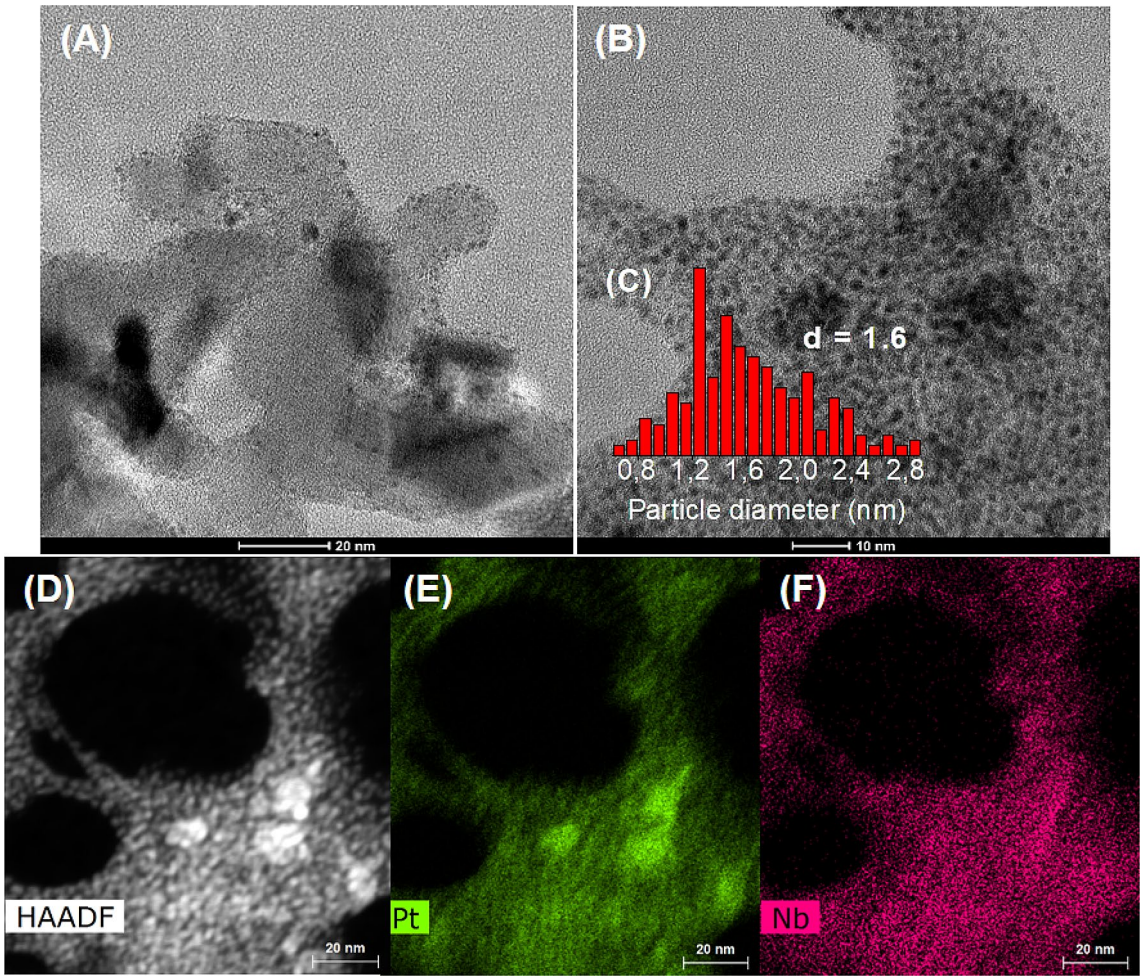

Fig. 2 Bright-field (BF) TEM image of **a** 26.6% Pt–NbO_x/TiN, **b** 100% Pt–NbO_x electrocatalyst, **c** particle size distribution, **d** HAADF TEM image of Pt–NbO_x nanoparticles, **e** EDS mapping of platinum and **f** EDS mapping of Nb

from 0.6 to 2.9 nm (Fig. 2c). HAADF imaging and STEM-EDS elemental mapping, as shown in Fig. 2d–f, revealed clear signs of overlap between Pt- and Nb-rich regions suggesting good mixing and uniform distribution of Pt and Nb on TiN support.

XRD pattern (Fig. S1) confirmed that TiN particles were successfully deposited by RSDT. The absence of peaks related to Pt and NbO_x phases can be related to their small particle size and the likely low crystallinity. Diffuse rings observed in selected area electron diffraction (SAED) pattern from TEM analysis (Fig. S2) confirmed the low crystallinity of Pt–NbO_x nanoparticles produced by RSDT. The peak position of TiN peaks in the XRD pattern of Pt–NbO_x/TiN deposited by RSDT on Si shifted slightly when compared to the as-received TiN precursor nanoparticles (Table 2). The lattice constant calculated from Bragg's Law was 4.241 Å for the precursor TiN nanoparticles and 4.229 Å for TiN nanoparticles after RSDT deposition. The lattice constant of the precursor TiN nanoparticles is the same constant reported for the cubic TiN phase (4.241 Å), while the lattice constant of RSDT TiN nanoparticles is between the cubic TiN phase (4.241 Å) and TiO phase (4.185 Å) [33].

Table 2 XRD peak position, crystallite size, and lattice constant

Sample	TiN peak/position (2θ)		Lattice constant (Å)
TiN standard [33]	(1 1 1)	36.673	4.241
	(2 0 0)	42.601	
	(2 2 0)	61.825	
TiN nanoparticles	(1 1 1)	36.653	4.241
	(2 0 0)	42.610	
	(2 2 0)	61.823	
TiN RSDT	(1 1 1)	36.770	4.229
	(2 0 0)	42.729	
	(2 2 0)	61.791	

Titanium oxynitride (TiO_xN_y) is an intermediate phase and it can be considered a solid solution of titanium nitride (TiN) and a cubic titanium oxide (TiO) [4, 34]. The lattice constant of RSDT TiN nanoparticles indicates there is replacement of some nitrogen atoms for oxygen atoms in the surface of TiN nanoparticles, which corroborates to a formation of oxynitride near the particle surface during RSDT deposition. As the titanium oxide is more thermodynamically stable than titanium nitride, an oxide or oxynitride layer is expected to form at the surface of TiN nanoparticles at room temperature, therefore, even under the relatively mild RSDT deposition conditions (80 °C) the potential oxidation of TiN is expected.

Raman Spectroscopy analysis (Figs. S3 and S4) corroborated with XRD results. Raman bands of cubic TiN were shown in three regions: the first in between 150 and 250 cm^{-1} corresponding to transverse acoustic mode, the second in between 250 and 350 cm^{-1} corresponding to longitudinal acoustic mode and the third in between 450 and 700 cm^{-1} corresponding to transverse optical mode in accordance with literature [35–38]. Raman lines of TiN nanoparticles processed by RDST were slightly shifted to lower frequencies compared to as purchased TiN nanoparticles (Fig. S3), which is expected to be a result of a decrease in the lattice parameter [9].

Electronic structure of Pt–NbO_x/TiN catalyst

XPS measurements were performed to evaluate the elemental composition and oxidation state of the surface of TiN and Pt–NbO_x/TiN catalyst (Figs. 3, 4, 5, 6, 7, 8). The XPS survey of TiN nanoparticles proceeds by RSDT (Fig. 3a) which indicates that the majority of atoms near the surface are titanium (25.3 wt%), fluorine (24.7 wt%), carbon (15.3 wt%), oxygen (14.3 wt%) and nitrogen (6.1 wt%). Fluorine and carbon come from the slurry dispersion, which contains Nafion™ and titanium and nitrogen from TiN nanoparticles. High-resolution XPS spectra were collected for the binding energy of Ti 2p, N 1 s and O 1 s (Figs. 4, 5, 6) and the peak assignments are shown in Table S1. Ti 2p spectra showed that Ti is present as TiN, TiO_xN_y, and TiO_2. The peak assignments of Ti $2p_{3/2}$ and Ti $2p_{1/2}$ shown in Table S1 were based on the literature [39–41]. This result suggests that the surface of TiN nanoparticles underwent oxidation during RSDT deposition, which is also supported by the results of XRD analysis (Table 2) and Raman spectroscopy (Fig. S3).

The XPS survey of 5.5% Pt–NbO_x/TiN (Fig. 3b) indicates that the majority of atoms near the surface are titanium (29.7 wt%), with catalysts Pt and Nb present in smaller amounts: 2.5 and 2.1 wt% respectively. High-resolution XPS spectra were collected for the binding energy of Ti 2p, N 1 s, O 1 s, Pt 4f and Nb 3d, (Figs. 4, 5, 6, 7, 8) and the peak assignments are shown in Table S1. The Pt 4f spectra (Fig. 7) were fit with peaks corresponding to the $4f_{7/2}$ and $4f_{5/2}$ states. The binding energy of the Pt $4f_{7/2}$ dominant peak was 72.4 eV, which is close to the value reported for PtO [42], the binding energy of the smaller peak (73.9 eV) is slight lower than the 74.4 eV reported for PtO_2 [42, 43]. The formation of Pt–O bonds is a result of the electron transfer from platinum to Nb_2O_5 [44]. The geometrical mismatch between Pt and Nb_2O_5 and the small size of Pt nanoparticles contribute to the strong metal–metal oxide interactions [19, 45]. The 5.5% Pt–NbO_x/TiN electrocatalyst has higher ratio of TiN support to Pt–NbO_x particles and the Pt–TiN interaction has major role. As a result, B.E. shifts towards lower energy due to charge transfer from the TiN support to platinum nanoparticles as reported by Roca-Ayats et al. [46, 47].

Nb 3d spectrum is a simple spin–orbit doublet with peaks corresponding to $Nb3d_{5/2}$ and $Nb3d_{3/2}$ (Fig. 8). The binding energy of the main peak at 208.06 eV agrees with Nb^{5+}, which has a binding energy of 207.8 eV, as reported by Morris et al. [48]. The small size of Pt–NbO_x nanoparticles contributes to shift $Nb3d_{5/2}$ peak to higher energy due to the screening effect of core holes and lattice strain as previously reported in the literature [49, 50]. Nb^{5+} was the dominant oxidation state, which suggests that Nb is mainly present as Nb_2O_5 near the surface. Ti 2p spectra showed that Ti is present as TiN, TiO_xN_y, and TiO_2 similar to the observation of the TiN nanoparticles processed by RSDT (Fig. 4).

As expected, the XPS survey scan of 26.6% Pt–NbO_x/TiN (Fig. 3c) showed a higher concentration of Pt and Nb atoms compared to 5.5% Pt–NbO_x/TiN. The absence of titanium and nitrogen peaks indicates that the Pt–NbO_x catalyst is covering the surface of the TiN support particles. High-resolution XPS spectra of 26.6% Pt–NbO_x/TiN were also collected for the binding energies of Ti 2p, N 1 s, O 1 s, Pt 4f and Nb 3d (Figs. 4, 5, 6, 7, 8). Ti 2p (Fig. 4) and N 1 s (Fig. 5) spectra had a significant decrease in intensity when compared to 5.5% Pt–NbO_x/TiN, which was related to the higher catalyst to support ratio and, as mentioned previously, to the fact that Pt–NbO_x catalyst are covering the TiN support particles. Furthermore, there was a displacement of peak position of Ti 2p, O 1 s, and N 1 s spectra of 26.6% Pt–NbO_x/TiN catalyst compared to 5.5% Pt–NbO_x/TiN and TiN (Table S1). The changes in O 1 s spectra are likely due to the higher amount of Nb_2O_5 in 26.6% Pt–NbO_x/TiN, which leads to higher Nb_2O_5 signal. The change in Ti 2p and N 1 s is an indicative of increased concentrations of TiO_2 and TiO_xN_y. During RSDT deposition, the substrate is heated in the range of 80–90 °C. This temperature is enough to promote surface oxidation of TiN nanoparticles [15]. As 26.6% Pt–NbO_x/TiN catalysts were deposited for a longer time, the TiN particles were subjected to elevated temperatures for a longer duration and were expected to have formed thicker surface oxide layers. This was confirmed

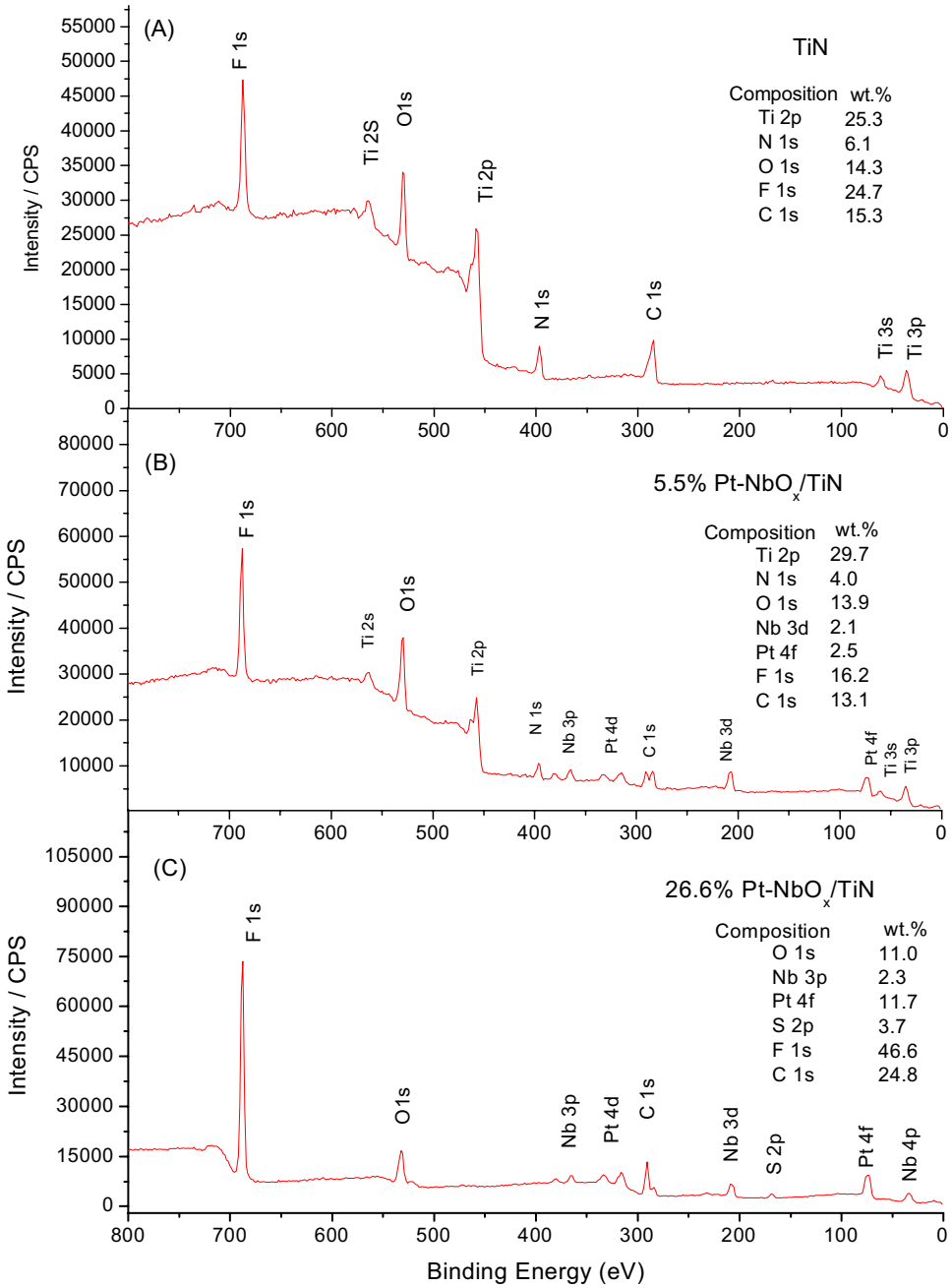

Fig. 3 XPS survey scan spectra of **a** TiN, **b** 5.5% Pt–NbO_x/TiN and **c** 26.6% Pt–NbO_x/TiN electrocatalysts

by the shift of the Raman lines to low frequencies in RSDT processed TiN nanoparticles (Fig. S3). The formation of the very stable oxynitride layer at TiN surface is expected to improve corrosion resistance and prevent further oxidation of TiN support during PEMFC operation. Therefore, TiN supports have the potential to improve support durability when compared to commercially available carbon-based supports [15]. The stability of the oxynitride layer on TiN was confirmed by analyzing samples after they had undergone electrochemical testing. Raman spectra of the samples after electrochemical testing showed no indication of significant change in oxide content (Fig. S4).

There is a slight change in the peak profile and a displacement of peaks positions to higher binding energy in the Pt 4f spectra of the 26.6% Pt–NbO_x/TiN electrocatalyst compared to the 5.5% Pt–NbO_x/TiN electrocatalyst (Table S1). The 26.6% Pt–NbO_x/TiN electrocatalyst has smaller ratio of TiN support to Pt–NbO_x nanoparticles and the Pt–TiN interaction has no significant effect on the peak position. On the other hand, the Pt–NbO_x interaction and small size of Pt nanoparticles play a major role resulting in the Pt 4f spectra shift towards higher energy [49, 50].

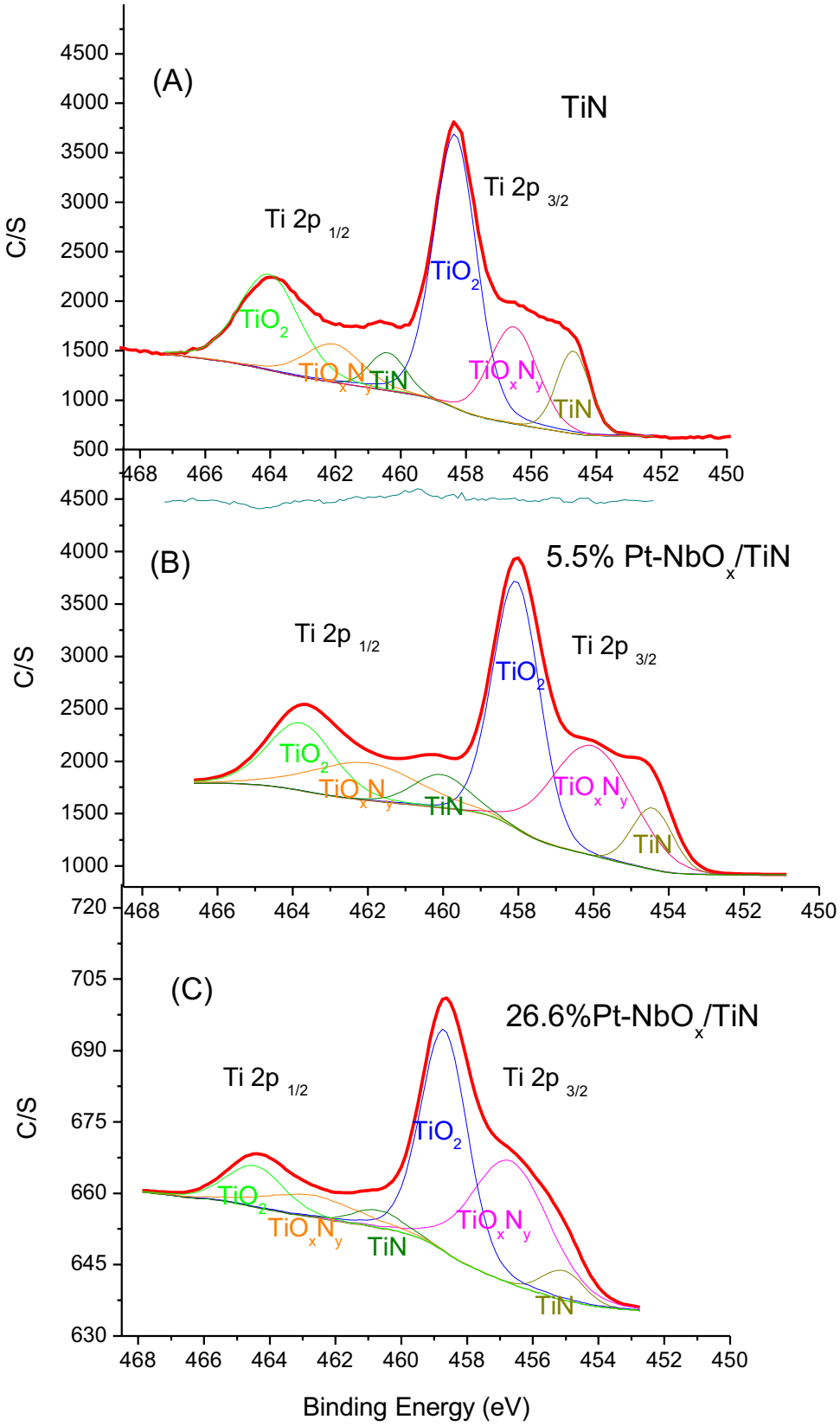

Fig. 4 High-resolution XPS spectra showing Ti 2p of **a** TiN, **b** 5.5% Pt–NbO_x/TiN and **c** 26.6% Pt–NbO_x/TiN electrocatalysts

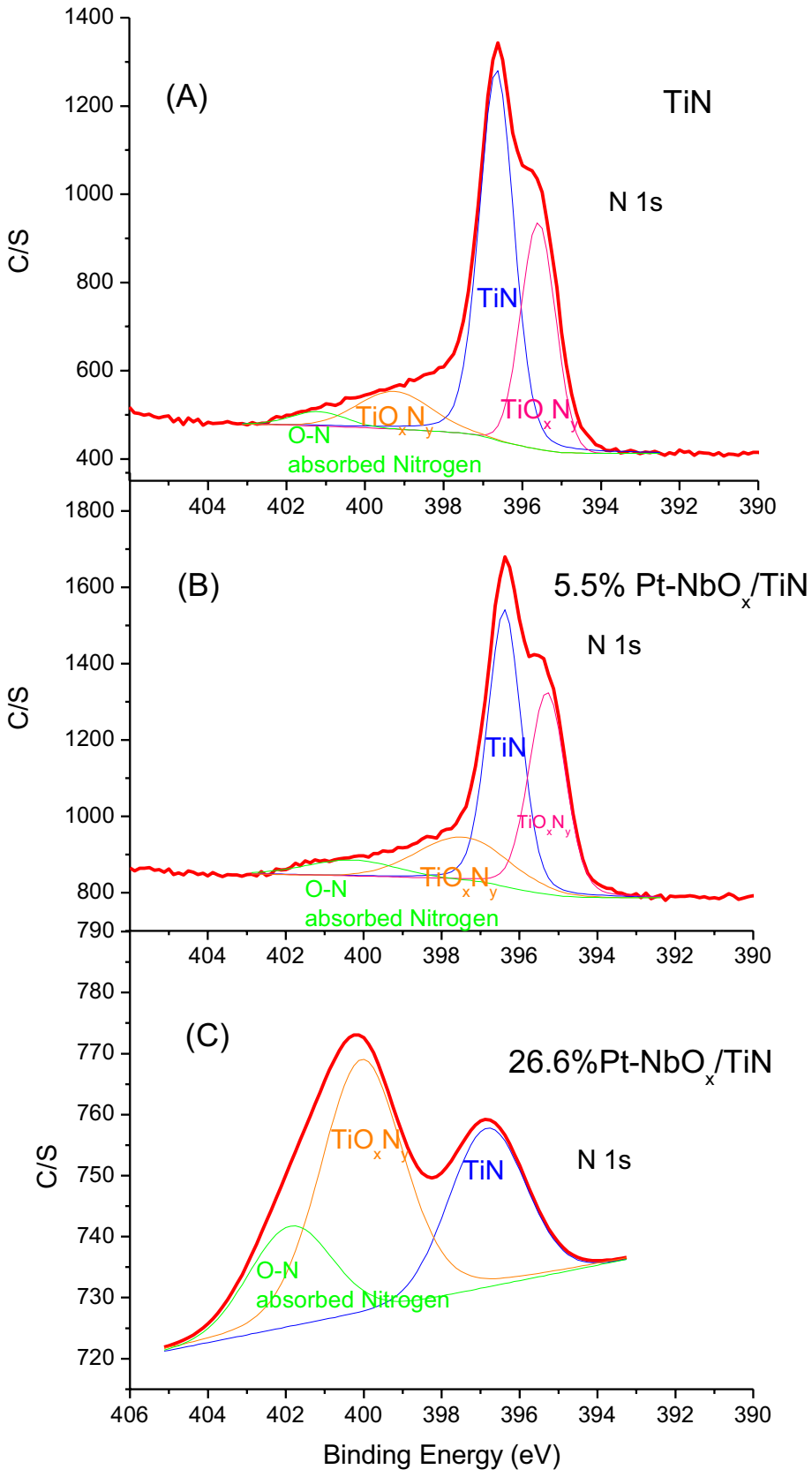

Fig. 5 High-resolution XPS spectra showing N s of **a** TiN, **b** 5.5% Pt–NbO_x/TiN and **c** 26.6% Pt–NbO_x/TiN electrocatalysts

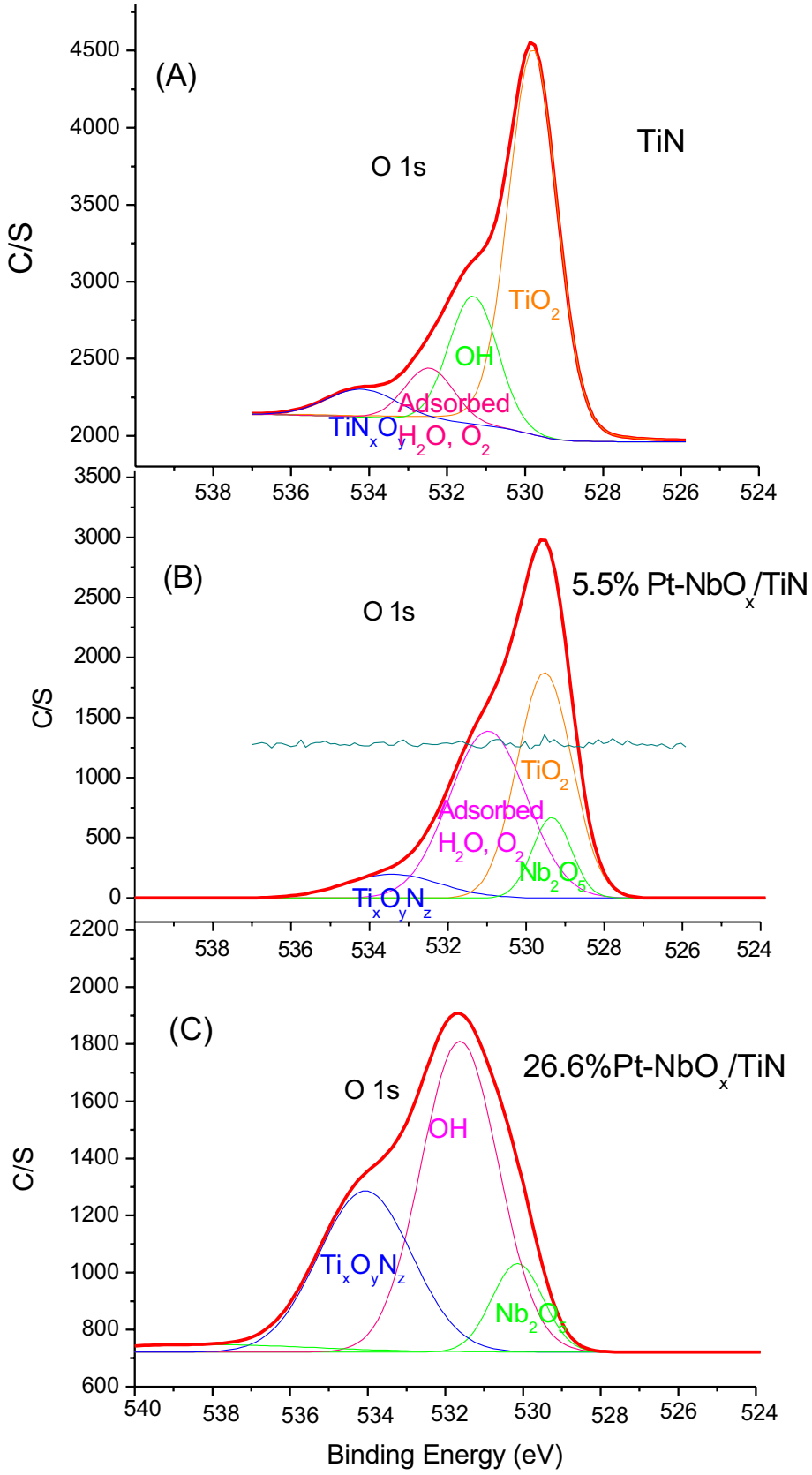

Fig. 6 High-resolution XPS spectra showing O s of **a** TiN, **b** 5.5% Pt–NbO_x/TiN and **c** 26.6% Pt–NbO_x/TiN electrocatalysts

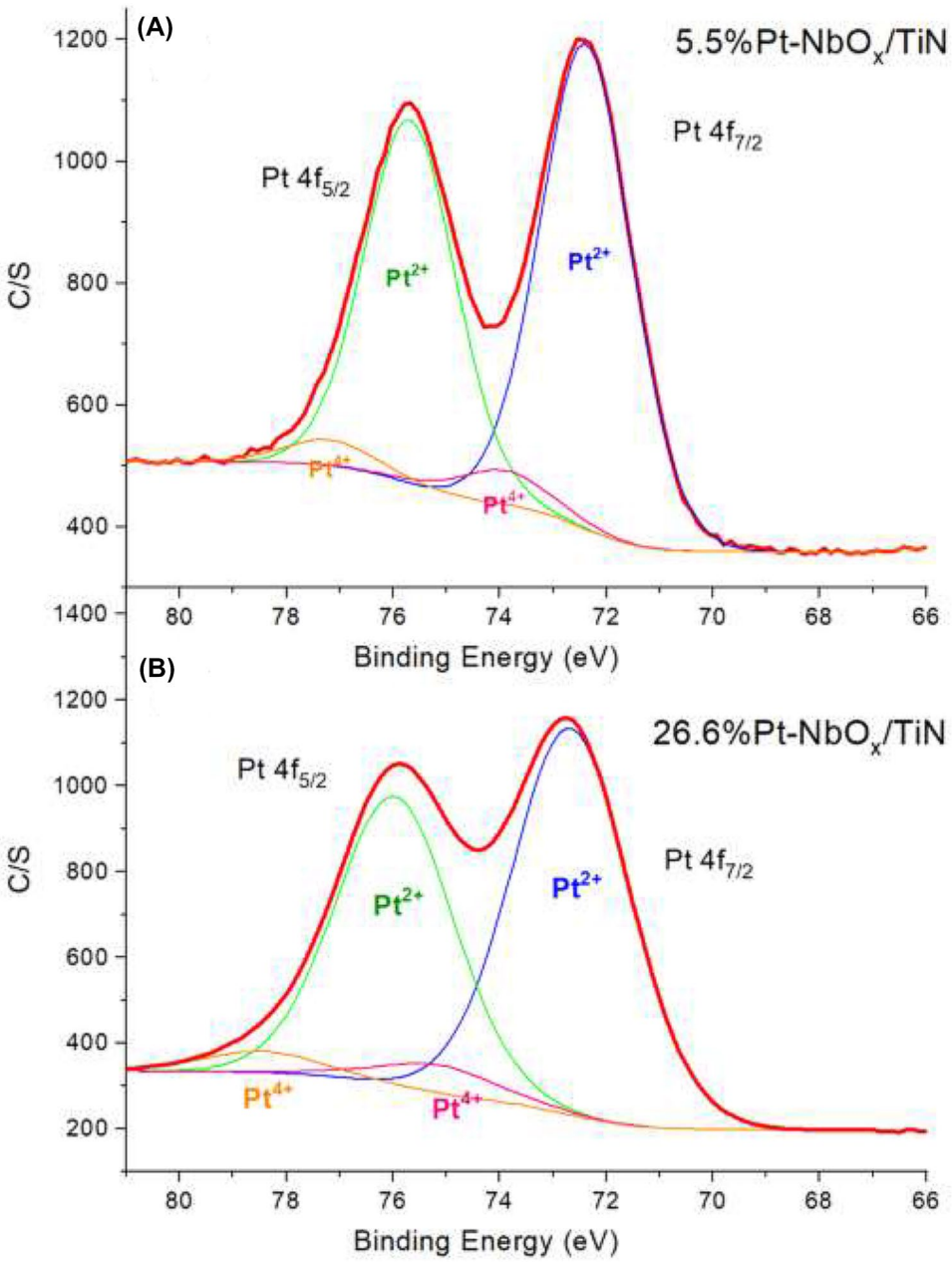

Fig. 7 High-resolution XPS spectra showing Pt 4f of **a** 5.5% Pt–NbO_x/TiN and **b** 26.6% Pt–NbO_x/TiN electrocatalysts

Electrochemical performance

RDE test was performed to study the electrochemical behavior of the Pt–NbO_x/TiN catalyst synthesized by the RSDT process. As the new catalyst has the potential for cathode catalyst application, ORR was investigated. ORR polarization curves for Pt–NbO_x/TiN electrocatalysts are shown in Fig. 9a. A half-wave potential in the ORR polarization curves of 790 mV was achieved for 5.5% Pt–NbO_x/TiN samples (Pt loading of 0.032 mg cm^{-2}) and 910 mV for 26.6% Pt–NbO_x/TiN (Pt loading 0.077 mg cm^{-2}). As expected, the half-wave potential increased with increased Pt loading, and a higher potential of those reported for Pt/C (880–900 mV) [32, 51–53] was achieved. The specific activity calculated with kinetic current i_k at 0.9 V vs RHE for the 26.6% Pt–NbO_x/TiN electrocatalyst was found to be 283 μA•cm_{Pt}^{-2}, which is also higher than those reported for Pt/C produced by RSDT at similar processing parameters [51] (Table 3). The higher half-wave potential and specific activity indicate that the modification in the structural and electronic state of Pt due to strong metal–metal oxide interactions among Pt, NbO_x and that TiN positively affects catalytic activity toward ORR, which is in good alignment with the findings from Zheng et al. [8], Goshal et al. [18], Jia et al. [19] and Chinchila et al. [54] for the

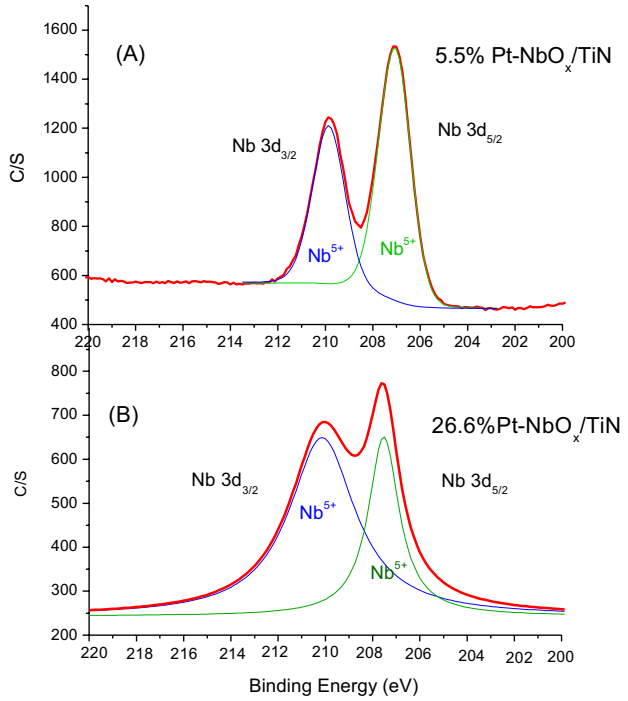

Fig. 8 High-resolution XPS spectra showing Nb 3d of **a** 5.5% Pt–NbO_x/TiN and **b** 26.6% Pt–NbO_x/TiN electrocatalysts

Pt–NbO_x interactions and Ding et al. [9] and Zheng et al. [55] for Pt–TiN_xO_y interactions.

The mass activity calculated from ORR curves and Pt loading of the catalyst (Table 3) was found to be 0.0194 and 0.120 A•mg_{Pt}^{-1} for the 5.5% Pt–NbO_x/TiN and 26.6% Pt–NbO_x/TiN electrocatalysts, respectively, which remain smaller than the 0.157 A•mg_{Pt}^{-1} and 0.21 A•mg_{Pt}^{-1} reported for Pt/C [32, 51]. In spite of the lower mass activity, it is expected that the Pt–NbO_x/TiN electrocatalyst will be more durable than the Pt/C catalyst and will keep its mass activity after many cycles. Because TiN oxidation forms TiO_2, which is solid, while C oxidation forms a gas CO_2, which leads to severe loss of the carbon support and the mass activity decreases due to the isolation of the Pt catalyst particles [15].

Two distinct Tafel regions, which are typical for the ORR at Pt electrocatalysts in acidic media [56], were observed (Fig. 9b). For the 5.5% Pt–NbO_x/TiN electrocatalyst, Tafel slopes of 72 mV dec^{-1} and 114.8 mV dec^{-1} were found at high (0.9–0.94 V) mV dec^{-1} and low (0.82–0.86 V) potentials, respectively. While, for the 26.6% Pt–NbO_x/TiN electrocatalyst, Tafel slopes of 62 mV dec^{-1} and 122 mV dec^{-1} were found at high (0.9–0.94 V) and low (0.80–0.84 V) potential, respectively. The ORR on Pt in acid media follows a dissociative adsorption of O_2, which is the rate-determining step. According to Banham et al. [56], the two distinct Tafel regions indicate that the rate-determining step (RDS) has changed from a rapid first electron transfer step at low potential to a slow first rapid first electron transfer step at high potential. At low potentials, the first electron step is the adsorption of reaction intermediates following Temkin isotherm. At high potential, the adsorption of reaction intermediates follows Langmuir isotherm as the catalyst surface is oxide free; thus, a different Tafel slope is measured.

The mass-corrected transport Tafel plots (Fig. 9b) and Tafel slopes of Pt–NbO_x/TiN electrocatalysts were similar to those reported for Pt/C (Table 3), indicating no change in the ORR mechanism. The total number of electrons transferred (n) during ORR was determined from Koutecky–Levich plots (Fig. S5) and it was found to be 3.9 at 0.4–0.7 V for 5.5% Pt–NbO_x/TiN and 3.7 at 0.3–0.85 V for 26.6% Pt–NbO_x/TiN. The values of n were close to 4, which confirms the ORR mechanism is similar to the Pt/C-based electrocatalyst.

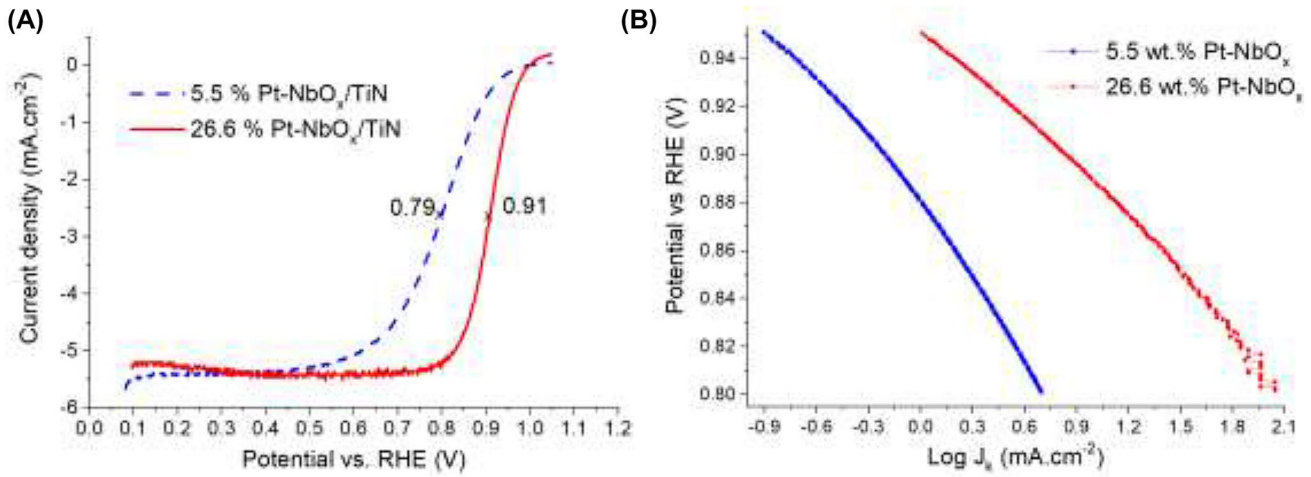

Fig. 9 ORR polarization curves **a** and Tafel plots **b** versus RHE recorded at 1600 rpm, at room temperature in O_2-saturated 0.1 M $HClO_4$

Table 3 Activity for oxygen reduction reaction obtained by RDE

Sample	Pt loading ($mg \cdot cm^{-2}$)	Half-wave potential (V)	ECSA ($m^2 gPt^{-1}$)	Specific activity I_s (0.9 V) ($\mu A\ cm_{Pt}^{-2}$)	Mass activity I_m (0.9 V) ($A\ mg_{Pt}^{-1}$)	Tafel slope mV dec^{-1}
5.5% Pt–NbO_x/TiN	0.032	0.79	–	–	0.0194	72 **(0.9–0.94 V)** 114.8 **(0.82–0.86 V)**
26.6% Pt–NbO_x/TiN	0.077	0.91	42.4	283	0.120	62 **(0.9–0.94 V)** 122 **(0.80–0.84 V)**
20% Pt/ C [32]	0.020	0.89	61	347	0.210	–
Pt/Vulcan [51]	0.020	0.88	65.4	248	0.157	64.9/126
19.7 Pt/Vulcan [52]	0.020	0.90	61	511	0.084	–
20% Pt/Vulcan [53]	0.065	0.90	48.3	600	0.290	–
46.4 wt% Pt/HSC (TKK) [57]	0.018	0.90	99	500	0.028	–
20% Pt/TiN [58]	0.020	0.81	75.6	21.7	0.016	–
5% Pt/TiN [59]	0.053	0.84	94	606	0.57	–

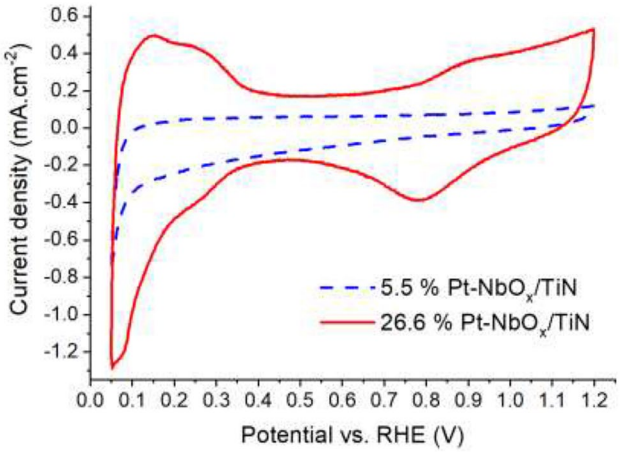

Fig. 10 Cycle voltammograms of 5.5% Pt–NbO_x/TiN and 26.6% Pt–NbO_x/TiN versus RHE collected at room temperature in N_2 statured 0.1 M H ClO_4 at sweep of 20 mV s^{-1}

The voltammetric profile of Pt–NbO_x/TiN electrocatalysts is shown in the cycle voltammograms (CV) in Fig. 10. The catalyst with a 5.5% Pt–NbO_x/TiN composition had limited hydrogen adsorption and desorption, so that they behaved similarly to pure TiN [39]. The poor catalytic activity is due to the low catalytic surface area which is suspected to result from the presence of relatively fewer number of Pt–NbO_x particles which was evident from the XPS measurements. Nevertheless, the catalyst with a 26.6% Pt–NbO_x/TiN composition exhibits a typical CV with distinct H adsorption/desorption peaks ($Pt + H_3O + \leftrightarrow Pt - H_{ad} + H_2O$) between 0.05 and 0.35 V. The higher activity is related to higher Pt loading in 26.6% Pt–NbO_x/TiN catalyst.

The electrochemical surface area (ECSA) derived from H adsorption was found to be 42.4 $m^2 gPt^{-1}$ for 26.6% Pt–NbO_x/TiN (Table 3). ECSA was not calculated for 5.5% Pt–NbO_x/TiN because there is no hydrogen desorption peak in CV (Fig. 10). The lower ECSA of 26.6% Pt–NbO_x/TiN in comparison with the values of Pt/C reported in the literature [51–53] is most likely due to the presence of niobium oxides in the surface as well as the oxidation of TiN support. The formation of an oxide layer in TiN support can partially cover the catalyst particles. On the other hand, this oxide layer may encapsulate Pt particles and thus avoid Pt migration and agglomeration during PEMFC operation thus increasing the catalyst's lifetime. Long-term tests are planned to investigate the durability of the catalyst. A compromise must be found between surface-active area and durability. The higher ORR activity in spite of low ECSA may be attributed to Pt and NbO_x interactions as discussed by Goshal et al. [18]. Nb oxide is expected to affect the activity of Pt due to strong metal–metal oxide interaction, thus increasing electrochemical stability.

The electrochemical performance (half-wave potential in ORR curves and H desorption in the CV curves) increases after running a few RDE tests. One hypothesis is that oxides, formed on the catalyst surface, dissociate at certain potentials, which increase Pt surface area and, therefore, catalytic activity. The remaining challenge is the TiN oxidation, which tends to decrease electrical conductivity as previously reported by Qiu et al. [60]. One alternative to improve conductivity is optimizing support particle shape. For instance, in the literature, the use of nanorods [61] or nanotubes [9, 17] is reported as a strategy to improve conductivity of the Pt/TiN electrocatalyst by increasing contact between TiN particles.

Conclusions

In this work, we reported a new electrocatalyst based on Pt–NbO_x supported on TiN nanoparticles. The capability of Pt–NbO_x/TiN catalyst fabrication in a single step by RSDT was demonstrated. TEM and XRD confirmed the synthesis of a well-dispersed Pt–NbO_x catalyst with an average

particle size of 1.6 nm diameter supported on TiN particles with a 20 nm diameter. The electrochemical performance was evaluated for ORR using the RDE method. Strong metal–metal oxide interactions between Pt and Nb oxide as well as between Pt and TiN_xO_y were observed in XPS analysis and may contribute to avoid Pt dissolution. A half-wave potential of 910 mV and a specific activity of 283 $\mu A \bullet cm_{Pt}^{-2}$ at 0.9 V was achieved in the new Pt–NbO_x/TiN electrocatalyst with a composition of 26.6% Pt–NbO_x/TiN which is higher than those reported for the state-of-the-art Pt/C. However, the ECSA of Pt–NbO_x/TiN electrocatalyst is still lower than the state-of-the-art Pt/C electrocatalyst. Therefore, based in previous studies about Pt/TiN systems, future work on the use of TiN particles with nanotubes or nanowire shapes is suggested as an alternative to increase ECSA.

This is the first report on a Pt–NbO_x/TiN electrocatalyst. The results achieved so far demonstrate that Pt/Nb–Nb_2O_5 loaded on TiN supports is a promising electrocatalyst for ORR in PEMFC. Further investigations to evaluate long-term performance as well as the performance of this catalyst in PEMFC tests will be presented in an ongoing study. As TiN is a more robust and stable support than carbon supports, it is expected that the Pt–NbO_x/TiN electrocatalyst will have higher durability than the carbon-supported electrocatalyst. Furthermore, the strong metal–metal oxide interactions between Pt and NbO_x and TiN_xO_y also require further analysis to optimize electrocatalyst performance and durability.

Acknowledgements N.F. Daudt acknowledges the Fulbright Program for the 4-month grant for her stay at the Center for Clean Energy Engineering at the University of Connecticut.

Compliance with ethical standards

Conflict of interest The authors declare that they have no conflict of interest.

References

1. Marcinkoski, J., Spendelow, J., Papageorgopoulos, D.: DOE Hydrogen and Fuel Cells Program Record (2015). https://www.hydrogen.energy.gov/pdfs/15015_fuel_cell_system_cost_2015.pdf. Accessed 15 Dec 2018
2. Chen, H., Song, Z., Zhao, X., Zhang, T., Pei, P., Liang, C.: A review of durability test protocols of the proton exchange membrane fuel cells for vehicle. Appl. Energy **224**, 289–299 (2018). https://doi.org/10.1016/j.apenergy.2018.04.050
3. Wang, Y., Chen, K.S., Mishler, J., Cho, S.C., Adroher, X.C.: A review of polymer electrolyte membrane fuel cells: technology, applications, and needs on fundamental research. Appl. Energy **88**(4), 981–1007 (2011). https://doi.org/10.1016/j.apenergy.2010.09.030
4. Avasarala, B., Moore, R., Haldar, P.: Surface oxidation of carbon supports due to potential cycling under PEM fuel cell conditions. Electrochim. Acta **16**(30), 4765–4771 (2010). https://doi.org/10.1016/j.electacta.2010.03.056
5. Huang, S.Y., Ganesan, P., Park, K., Popov, B.N.: Development of a titanium dioxide-supported platinum catalyst with ultrahigh stability for polymer electrolyte membrane fuel cell applications. J. Am. Chem. Soc. **131**(39), 13898–13899 (2009). https://doi.org/10.1016/j.apcatb.2010.02.025
6. Huang, S.Y., Ganesan, P., Popov, B.N.: Electrocatalytic activity and stability of niobium-doped titanium oxide supported platinum catalyst for polymer electrolyte membrane fuel cells. Appl. Catal. B **96**, 224–231 (2010). https://doi.org/10.1016/j.apcatb.2010.02.025
7. Senevirathne, K., Neburchilov, V., Alzate, V., Baker, R., Neagu, R., Zhang, J., Campbell, S., Ye, S.: Nb-doped TiO_2/carbon composite supports synthesized by ultrasonic spray pyrolysis for proton exchange membrane (PEM) fuel cell catalysts. J. Power Sour. **220**, 1–9 (2012). https://doi.org/10.1016/j.jpowsour.2012.07.080
8. Zeng, Y., Guo, X., Wang, Z., Geng, J., Zhang, H., Song, W., Yu, H., Shao, Z., Yia, B.: Highly stable nanostructured membrane electrode assembly based on Pt/Nb_2O_5 nanobelts with reduced platinum loading for proton exchange membrane fuel cells. Nanoscale **9**, 6910–6919 (2017). https://doi.org/10.1039/C7NR01491K
9. Ding, Z., Cheng, Q., Zou, L., Fang, J., Zou, Z., Yang, H.: Controllable synthesis of titanium nitride nanotubes by coaxial electrospinning and their application as a durable support for oxygen reduction reaction electrocatalysts. Chem. Commun. **53**, 13233–13236 (2017). https://doi.org/10.1039/C7CC08151K
10. Xiao, Y., Zhan, G., Fu, Z., Pan, Z., Xiao, C., Wu, S., Chen, C., Hu, G., Wei, Z.: Robust non-carbon titanium nitride nanotubes supported Pt catalyst with enhanced catalytic activity and durability for methanol oxidation reaction. Electrochim. Acta **141**, 279–285 (2014). https://doi.org/10.1016/j.electacta.2014.07.070
11. Kumar, R., Pasupathi, S., Pollet, B.G., Scott, K.: Nafion-stabilised platinum nanoparticles supported on titanium nitride: an efficient and durable electrocatalyst for phosphoric acid based polymer electrolyte fuel cells. Electrochim. Acta **109**, 365–369 (2013). https://doi.org/10.1016/j.electacta.2013.07.140
12. Seifitokaldani, A., Savadogo, O.: Electrochemically stable titanium oxy-nitride support for platinum electro-catalyst for PEM fuel cell applications. Electrochim. Acta **167**, 237–245 (2015). https://doi.org/10.1016/j.electacta.2015.03.189
13. Cui, Z., Burns, R.G., DiSalvo, F.J.: Mesoporous $Ti_{0.5}Nb_{0.5}N$ ternary nitride as a novel noncarbon support for oxygen reduction reaction in acid and alkaline electrolytes. Chem. Mater. **25**, 3782–3784 (2013). https://doi.org/10.1021/cm4027545

14. Kim, J.H., Kwon, G., Lim, H., Zhu, C., You, H.: Effects of transition metal doping in Pt/M–TiO_2 (M = V, Cr, and Nb) on oxygen reduction reaction activity. J. Power Sour. **320**, 188–195 (2016). https://doi.org/10.1016/j.jpowsour.2016.04.019
15. Avasarala, B., Haldar, P.: Durability and degradation mechanism of titanium nitride based electrocatalysts for PEM (proton exchange membrane) fuel cell applications. Energy **57**, 545–553 (2013). https://doi.org/10.1016/j.energy.2013.05.021
16. Avasarala, B., Haldar, P.: On the stability of TiN-based electrocatalysts for fuel cell applications. Int. J. Hydrogen Energy **36**, 3965–3974 (2011). https://doi.org/10.1016/j.ijhydene.2010.12.107
17. Shin, H., Kim, H., Chung, D.Y., Yoo, J.M., Weon, S., Choi, W., Sung, Y.E.: Scaffold-like titanium nitride nanotubes with a highly conductive porous architecture as a nanoparticle catalyst support for oxygen reduction. ACS Catal. **6**, 3914–3920 (2016). https://doi.org/10.1021/acscatal.6b00384
18. Goshal, S., Jia, Q., Bates, M.K., Li, J., Xu, C., Gath, K., Yang, J., Waldecker, J., Che, H., Liang, W., Meng, G., Ma, Z.F., Mukerjee, S.: Tuning Nb−Pt interactions to facilitate fuel cell electrocatalysis. ACS Catal. **7**(8), 4936–4946 (2017). https://doi.org/10.1021/acscatal.7b01061
19. Jia, Q., Ghoshal, S., Li, J., Liang, W., Meng, G., Che, H., Zhang, S., Ma, Z.F., Mukerjee, S.: Metal and metal oxide interactions and their catalytic consequences for oxygen reduction reaction. J. Am. Chem. Soc. **139**(23), 7893–7903 (2017). https://doi.org/10.1021/jacs.7b02378
20. Alvar, E.N., Zhou, B., Eichhorn, S.H.: Carbon-embedded mesoporous Nb-doped TiO_2 nanofibers as catalyst support for the oxygen reduction reaction in PEM fuel cells. J. Mater. Chem. A **4**, 6540–6552 (2016). https://doi.org/10.1039/C5TA08801A
21. Burk, J.J., Buratto, S.K.: Electrodeposition of Pt nanoparticle catalysts from H2Pt(OH)6 and their application in PEM fuel cells. J. Phys. Chem. C **117**(37), 18957–18966 (2013). https://doi.org/10.1021/jp405302x
22. Saibuathong, N., Saejeng, Y., Pruksathorn, K., Hunsom, M., Tantavichet, N.: Catalyst electrode preparation for PEM fuel cells by electrodeposition. J. Appl. Electrochem. **40**(5), 903–910 (2010). https://doi.org/10.1007/s10800-009-9965-4
23. Fiala, R., Vaclavu, M., Vorokhta, M., Khalakhan, I., Lavkova, J., Potin, V., Matolinova, I., Matolin, V.: Proton exchange membrane fuel cell made of magnetron sputtered Pt–CeOx and Pt–Co thin film catalysts. J. Power Sour. **273**, 105–109 (2015). https://doi.org/10.1016/j.jpowsour.2014.08.093
24. Ernst, F.O., Büchel, R., Strobel, R., Pratsinis, S.E.: One-step flame-synthesis of carbon-embedded and supported platinum clusters. Chem. Mater. **20**, 2117–2123 (2008). https://doi.org/10.1016/j.jpowsour.2014.08.093
25. Strobel, R., Pratsinis, S.E.: Flame synthesis of supported platinum group metals for catalysis and sensors. Platin. Met. Rev **53**(1), 11 (2009). https://doi.org/10.1595/147106709X392993
26. Maric, R.: Spray-based and CVD processes for synthesis of fuel cell catalysts and thin catalyst layers. In: Zhang, J. (ed.) PEM fuel cell electrocatalysts and catalyst layers. Springer, London (2008). https://doi.org/10.1007/978-1-84800-936-3_20
27. Maric, R., Roller, J., Neagu, R.: Flame-based technologies and reactive spray deposition technology for low-temperature solid oxide fuel cells. J. Therm. Spray Technol. **20**, 696–718 (2011). https://doi.org/10.1007/s11666-011-9645-x
28. Yu, H., Roller, J.M., Mustain, W.E., Maric, R.: Influence of the ionomer/carbon ratio for low-Pt loading catalyst layer prepared by reactive spray deposition technology. J. Power Sour. **283**, 84–95 (2015). https://doi.org/10.1016/j.jpowsour.2015.02.101
29. Yu, H., Baricci, A., Bisello, A., Casalegno, A., Guetaz, L., Bonville, L., Maric, R.: Strategies to mitigate Pt dissolution in low Pt loading proton exchange membrane fuel cell: I. A gradient Pt particle size design. Electrochim. Acta **247**(1), 1155–1168 (2017). https://doi.org/10.1016/j.electacta.2017.07.093
30. Roller, J.M., Kim, S., Kwak, T., Yu, H., Maric, R.: A study on the effect of selected process parameters in a jet diffusion flame for Pt nanoparticle formation. J. Mater. Sci. **52**, 9391–9409 (2017). https://doi.org/10.1007/s10853-017-1101-y
31. Schneider, C.A., Rasband, W.S., Eliceiri, K.W.: NIH image to ImageJ: 25 years of image analysis. Nat. Methods **9**(7), 671–675 (2012). https://doi.org/10.1038/nmeth.2089
32. Garsany, Y., Baturina, O.A., Swider-Lyons, K.E.: Experimental methods for quantifying the activity of platinum electrocatalysts for the oxygen reduction reaction. Anal. Chem. **82**(15), 6321–6328 (2010). https://doi.org/10.1021/ac100306c
33. Powder Diffraction File, Card Nos. 38-14120 (TiN) and 77-2170 (TiO). Joint Committee on Powder Diffraction Standards (JCPDS), Swarthmore, PA (1955)
34. Hyett, G., Green, M.A., Parkin, I.P.: The use of combinatorial chemical vapor deposition in the synthesis of $Ti_{3-\delta}O_4N$ with $0.06 < \delta < 0.25$: a titanium synthesis of Ti_3O_4N with $0.06 < \delta < 0.25$: a titanium. J. Am. Chem. Soc. **129**(9), 15541–15548 (2007). https://doi.org/10.1021/ja073355s
35. Ding, Z.H., Yao, B., Qiu, L.X., Lv, T.Q.: Raman scattering investigation of nanocrystalline δ-TiN_x synthesized by solid-state reaction. J. Alloy. Compd. **421**, 247–251 (2006). https://doi.org/10.1016/j.jallcom.2005.11.017
36. Wei, H., Wu, M., Dong, Z., Chen, Y.: Composition, microstructure and SERS properties of titanium nitride thin film prepared via nitridation of sol–gel derived titania thin films. J. Raman Spectrosc **48**, 578–585 (2017). https://doi.org/10.1002/jrs.5080
37. Achour, A., Porto, R.L., Soussou, M.A., Islam, M., Boujtita, M., Aissa, K.A., Le Brizoual, L., Djouadi, A., Brousse, T.: Titanium nitride films for micro-supercapacitors: effect of surface chemistry and film morphology on the capacitance. J. Power Sour. **300**, 525–532 (2015). https://doi.org/10.1016/j.jpowsour.2015.09.012
38. Kataria, S., Srivastava, S.K., Kumar, P., Siju, G.S., Khan, J., Sridhar Rao, D.V., Barshilia, H.C.: Nanocrystalline TiN coatings with improved toughness deposited by pulsing the nitrogen flow rate. Surf. Coat. Technol. **206**(19–20), 4279–4286 (2012). https://doi.org/10.1016/j.surfcoat.2012.04.040
39. Avasarala, B., Haldar, P.: Electrochemical oxidation behavior of titanium nitride based electrocatalysts under PEM fuel cell conditions. Electrochim. Acta **55**(28), 9024–9034 (2010). https://doi.org/10.1016/j.electacta.2010.08.035
40. Saha, N.C., Tompkins, H.G.: Titanium nitride oxidation chemistry: an X-ray photoelectron spectroscopy study. J. Appl. Phys. **72**, 3072–3079 (1992). https://doi.org/10.1063/1.351465
41. Chyou, S.D., Shih, H.C., Chen, T.T.: On the corrosion characterization of titanium nitride in sulfuric acid solution. Corros. Sci. **35**(1–4), 337–341 (1993). https://doi.org/10.1016/0010-938X(93)90165-D
42. Shukla, A.K., Neergat, M., Bera, P., Jayaram, V., Hegde, M.S.: An XPS study on binary and ternary alloys of transition metals with platinized carbon and its bearing upon oxygen electroreduction in direct methanol fuel cells. J. Electroanal. Chem. **504**(1), 111–119 (2001). https://doi.org/10.1016/S0022-0728(01)00421-1
43. Kim, K.S., Winograd, N., Davis, R.E.: Electron spectroscopy of platinum-oxygen surfaces and application to electrochemical studies. J. Am. Chem. Soc. **93**(23), 6296–9297 (1971). https://doi.org/10.1021/ja00752a065
44. Zhang, L., Wang, L., Holt, C.M.B., Navessin, T., Malek, K., Eikerling, M.H., Mitlin, D.: Oxygen reduction reaction activity and electrochemical stability of thin-film bilayer systems of platinum on niobium oxide. J. Phys. Chem. C **114**(39), 16463–16474 (2010). https://doi.org/10.1021/jp104306j

45. Mavrikakis, M., Stoltze, P., Nørskov, J.K.: Making gold less noble. Catal. Lett. **64**, 101–106 (2000). https://doi.org/10.1023/A:1019028229377
46. Roca-Ayats, M., GarcIa, G., Pena, M.A., Martınez-Huerta, M.V.: Titanium carbide and carbonitride electrocatalyst supports: modifying Pt–Ti interface properties by electrochemical potential cycling. J. Mater. Chem. A **2**, 18786–18790 (2014). https://doi.org/10.1039/C4TA03782K
47. Roca-Ayats, M., García, G., Galante, J.L., Peña, M.A., Martínez-Huerta, M.V.: TiC, TiCN, and TiN supported Pt electrocatalysts for CO and methanol oxidation in acidic and alkaline media. J. Phys. Chem. C **117**(40), 20769–20777 (2013). https://doi.org/10.1021/jp407260v
48. Morris, D., Dou, Y., Rebane, J., Mitchell, C.E.J., Egdell, R.G.: Photoemission and STM study of the electronic structure of Nb-doped TiO_2. Phys. Rev. B **61**(20), 13445–13457 (2000). https://doi.org/10.1103/PhysRevB.61.13445
49. Yu, H., Davydova, E.S., Ash, U., Miller, H.A., Bonville, L., Dekel, D.R., Maric, R.: Palladium-ceria nanocatalyst for hydrogen oxidation in alkaline media: optimization of the Pd–CeO_2 interface. Nano Energy **57**, 820–826 (2019). https://doi.org/10.1016/j.nanoen.2018.12.098
50. Mason, M.G.: Electronic structure of supported small metal clusters. Phys. Rev. B **27**(2), 748–762 (1983). https://doi.org/10.1103/PhysRevB.27.748
51. Yu, H., Baricci, A., Justin, R., Wang, Y., Casalegno, A., Mustain, W., Maric, R.: Ultra-low Pt loading catalyst layers for PEMFC using reactive spray deposition technology. ECS Trans. **69**(17), 487–496 (2015). https://doi.org/10.1149/06917.0487ecst
52. Garsany, Y., Singer, I.L., Swider-Lyons, K.E.: Impact of film drying procedures on RDE characterization of Pt/VC electrocatalysts. J. Electroanal. Chem. **662**(2), 396–406 (2011). https://doi.org/10.1016/j.jelechem.2011.09.016
53. van der Vliet, D., Wang, C., Debe, M., Atanasoski, R., Markovic, N.M., Stamenkovic, V.R.: Platinum-alloy nanostructured thin film catalysts for the oxygen reduction reaction. Electrochim. Acta **56**(24), 8695–8699 (2011). https://doi.org/10.1016/j.electacta.2011.07.063
54. Chinchilla, L., Rossouw, D., Trefz, T., Susac, D., Kremliakova, N., Botton, G.A.: Nanoscale analysis of structural and chemical changes in aged hybrid Pt/NbOx/C fuel cell catalysts. J. Power Sour. **356**, 140–152 (2017). https://doi.org/10.1016/j.jpowsour.2017.04.017
55. Zheng, Y., Zhang, J., Zhan, H., Suna, D., Dang, D., Tian, X.L.: Porous and three dimensional titanium nitride supported platinum as an electrocatalyst for oxygen reduction reaction. Electrochem. Commun. **91**, 31–35 (2018). https://doi.org/10.1016/j.elecom.2018.04.021
56. Banham, D.W., Soderberg, J.N., Birss, V.I.: Pt/carbon catalyst layer microstructural effects on measured and predicted Tafel slopes for the oxygen reduction reaction. J. Phys. Chem. C **113**(23), 10103–10111 (2009). https://doi.org/10.1021/jp809987g
57. Shinozaki, K., Zack, J.W., Richards, R.M., Pivovar, B.S., Kocha, S.S.: Oxygen reduction reaction measurements on platinum electrocatalysts utilizing rotating disk electrode technique. J. Electrochem. Soc. **162**(10), F1144–F1158 (2015). https://doi.org/10.1149/2.1071509jes
58. Avasarala, B., Murray, T., Li, W., Haldar, P.: Titanium nitride nanoparticles based electrocatalysts for proton exchange membrane fuel cells. J. Mater. Chem. **19**(15), 1803–1805 (2009). https://doi.org/10.1039/B819006B
59. Tian, X., Luo, J., Nan, H., Zou, H., Chen, R., Shu, T., Li, X., Li, Y., Song, H., Liao, S., Adzic, R.R.: Transition metal nitride coated with atomic layers of Pt as a low-cost, highly stable electrocatalyst for the oxygen reduction reaction. J. Am. Chem. Soc. **138**, 1575–1583 (2016). https://doi.org/10.1021/jacs.5b11364
60. Qiu, Y., Gao, L.: Novel polyaniline/titanium nitride nanocomposite: controllable structures and electrical/electrochemical properties. J. Phys. Chem. B **109**(42), 19732–19740 (2005). https://doi.org/10.1021/jp053845b
61. Jiang, S., Yi, B., Zhang, H., Song, W., Bai, Y., Yu, H., Shao, Z.: Vertically aligned titanium nitride nanorod arrays as supports of platinum–palladium–cobalt catalysts for thin-film proton exchange membrane fuel cell electrodes. Chem Electro Chem **3**, 734–740 (2016). https://doi.org/10.1002/celc.201500571